



The Effect of Protein Structure and Concentration on Tribocorrosion and Film Formation on CoCrMo Alloys

Mohamad Taufiqurrakhman¹ · Anne Neville¹ · Michael G. Bryant¹

Received: 15 February 2021 / Revised: 26 July 2021 / Accepted: 7 September 2021
© The Author(s) 2021

Abstract

The formation of tribochemical reaction layers, better known as tribofilms, on cobalt-chromium-molybdenum (CoCrMo) alloys commonly used in orthopaedic applications has been hypothesized to reduce degradation owing to wear and corrosion. However, the mechanisms and pathways influencing tribofilm formation remain largely unknown. This study aims to develop a clearer understanding of the role of protein structures and its concentration on tribocorrosion and surface tribofilms formed on CoCrMo alloys during boundary regime sliding. A reciprocating tribometer with a three-electrode electrochemical cell was employed to simulate and monitor the tribocorrosion of CoCrMo in situ. As-received Foetal Bovine Serum (as-FBS) and pre-heated FBS at 70 °C for 1 h (de-FBS) were diluted with saline (0.9% NaCl) at different concentrations (25% and 75% v/v) and utilized as electrolytes during the tribocorrosion tests. The result shows that the denatured protein structure in electrolyte tends to reduce the volume losses due to wear and corrosion on the CoCrMo samples with an appreciation of the protein tribofilms. On the other hand, an increased protein concentration increased the total volume loss due to corrosive processes. A novel finding revealed in this study is that the tribocorrosion mechanism of the CoCrMo surface is dependent on the protein structure, concentration and sliding duration due to the change in surface condition.

Keywords Serum protein · CoCrMo alloys · Tribocorrosion · Hip implant

1 Introduction

CoCrMo is one of the most widely used bearing materials in Total Hip Replacements (THR) owing to its excellent mechanical properties, self-mating performance and perceived biocompatibility [1–3]. However, the use of CoCrMo alloys is not without problems and issues associated with tribology, corrosion and implant-associated debris remain of interest to the community [4–6]. Tribocorrosion, the combined process of wear and corrosion, causes the simultaneous generation of metallic debris (mechanical wear) and ion release (electrochemical corrosion) [7, 8]. The release of metal products has been seen to elicit adverse biological reactions requiring surgical intervention and the revision of an existing implant [9–11]. Examples of tribocorrosion within orthopaedic applications include metal-on-metal (MoM) THR, MoM hip resurfacing and three-body abrasion

within metal-on-polymer bearings [12–14]. Whilst the second generation metal-on-metal hip replacements have largely been withdrawn from the market due to their higher than acceptable revision rates, MoM hip resurfacing is still being implanted and presents satisfactory results among certain patient demographics [15]. However, questions around the long-term risk associated with the implant derived debris, safety and longevity performance of metal-based implants remain [16–18].

Reduced wear and corrosion can only be achieved once the fundamental surface mechanisms are well understood [19]. The tribocorrosive mechanisms of CoCrMo surfaces has been investigated from in vivo retrieval implants [20] and in vitro tests [21] point of view. The results indicated that tribochemical reactions, chemical reactions activated by the tribological processes, are common on metallic surfaces when slid in protein containing electrolytes. It has been recently hypothesized that tribochemical reactions govern the formation or removal of chemical products or tribofilms at the mechanically mixed zone [22]. Tribofilms, which commonly contain organic carbon from pseudo-synovial fluid and metallic nanocrystalline material after mechanical

✉ Mohamad Taufiqurrakhman
moh.taufiqurrakhman@gmail.com

¹ Institute of Functional Surfaces (iFS), School of Mechanical Engineering, University of Leeds, Leeds LS2 9JT, UK

mixing, were found on the retrieved MoM bearings and thought to have a wear-reducing role [23]. Therefore, understanding the interactions between the contacting surfaces and biological fluid is crucial when determining the tribo-corrosive degradation of implant materials.

Proteins, the dominant molecule in (pseudo) synovial fluid, are composed of a complex structure of amino acids and stabilized by several interactions, such as covalent bonding (

e.g. disulfide bonds) and non-covalent bonding (e.g. electrostatic forces, hydrogen bonding and hydrophobic interaction) [24, 25]. The protein structure can be unfolded by denaturation; a process to modify the protein structure by decomposing the weak intermolecular bonds [26]. Studies have successfully characterized the protein denaturation after heat treatment [27, 28], mechanical shear [29], reactive metal surfaces [29], conditioned pH [30–32], diseases and chemically denaturation [33–36] using Raman spectroscopy. Protein structure can be effectively indicated by changes in the Raman shift, signal intensity and deconvolution of specific Raman shift bands; for instance, disulfide bonds and secondary structures [27, 37]. Proteins have been shown to interact (e.g. protein adsorption) with a metal surface, affecting the static and tribocorrosion properties [5, 17, 38–41].

Elevations in temperatures owing to the frictional shear of asperities at contacting interfaces, known as flash temperatures, are well described in the field of tribology [30]. However, the temperature parameter has received limited attention in the area of biotribology, despite the sensitivity of the lubricating environment [17]. Wimmer et al. [21] hypothesized that protein tribofilms are, in part, due to thermal degradation of proteins estimated flash temperatures within CoCrMo-CoCrMo contacts to be in the region of 55 °C. Furthermore, Bergmann et al. [42] reported that the implant temperature could reach a range of 20–60 °C, measured in vivo using an instrumented hip implant, and

depended on the walking cycles, speed and material combinations. Elevated temperatures (> 50 °C) have been shown to weaken and even break the disulfide chain, which results in an unstable secondary structure and the loss of protein biological activity [34, 35, 43]. It is therefore logical that the initial and subsequent tribochemical reactions occurring at contacting surfaces may be affected by the structure of the protein within the (pseudo) synovial fluid. Hence, it is essential to understand the underlying degradation mechanisms of metallic bearings when subjected to various protein conditions in the biological fluid.

Currently, no studies have used deliberately denatured protein structures as the testing electrolyte during tribocorrosion. Whilst previous studies have employed increasing external temperature to investigate the static corrosion of CoCrMo in protein containing environment [44, 45], the effects on denatured protein on the tribocorrosion processes remains largely unknown. Therefore, the aim of this study is to gain a clearer understanding of the effect of protein structures and its concentration on the tribocorrosion mechanism and surface tribofilms on CoCrMo alloys during boundary regime sliding. One of the novelties of this study is the fact that heat was used intentionally to break the protein structure and simulate the possibility of temperature changes occurring inside the human body via tribology at hard surfaces.

2 Materials and Methodology

A combination of tribocorrosion, surface and electrolyte analysis techniques were employed within this study. Figure 1 shows a schematic of the experimental protocol used in this study.

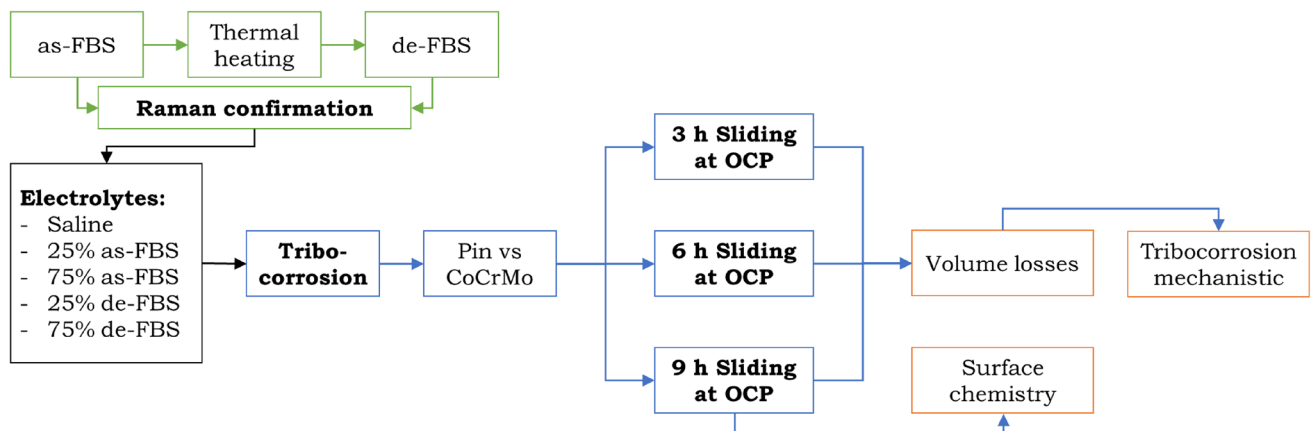


Fig. 1 Schematic of tribocorrosion tests and surface analysis protocols

2.1 CoCrMo Samples

Wrought low-carbon Co-28Cr-6Mo alloy (later abbreviated to CoCrMo) was used as a flat sample, according to the specification in ASTM F75-12 standard [46]. The alloy was supplied (Peter Brehm GmbH, Germany) as a 22 mm diameter rod which was cut into a flat component with 6 mm thickness. The samples were grounded by silicon carbide paper (grit sizes 600 to 1200) then mirror-polished by a 3 μm and $\frac{1}{4}$ μm diamond paste and polishing paper (Bruker Corporations, UK) to achieve an approximate surface $R_a \sim 5$ nm. After polishing, CoCrMo samples were degreased with acetone, rinsed with deionized (DI) water and dried under a compressed air stream. Samples were used for tribocorrosion testing directly after grinding procedures. This procedure is in line with others working within this field [47–50] and in line with ASTM G5 [51] and G59 [52] guidance.

2.2 Raman Confirmation and Electrolytes Preparation

Foetal Bovine Serum (FBS) (Sera Laboratories International, UK), triple 0.1 μM sterile filtered and European grade, was used as the testing electrolyte in this study. Bovine serum is a typical electrolyte used to simulate the proteins present in synovial fluid with such concentrations [53–55]. Figure 2a shows the heat treatment processes of FBS prior to dilution for tribocorrosion testing. A digitally controlled hotplate was used to heat the as-received FBS (as-FBS) at 70 $^{\circ}\text{C}$ for 1 h to produce pre-heated FBS (de-FBS). The heating temperature was chosen based on the flash temperatures estimated in vivo [29, 40, 56]. Following these tests, all heated FBS were taken (30 mL by syringe) and moved to Petri dishes for Raman spectroscopy purposes.

Raman spectroscopy was used to confirm the change in FBS structure after pre-heating at 70 $^{\circ}\text{C}$ for 1 h.

InVia Raman spectroscopy (Renishaw, UK) was utilized to confirm the protein structural changes of the de-FBS electrolyte. The Raman spectrometer has a lateral resolution of 800 nm and a spectral resolution of 1 cm^{-1} . It is equipped with 785 nm wavelength lasers (the radius laser spot is 640 nm) working at a 220 mW maximum laser power at the source. The Raman signals were acquired by an Olympus 50 \times objective with 0.75 numerical aperture for a backscattering configuration. The raw spectra were proceeded using WiRE 3.4 software (Renishaw, UK) to subtract the entire spectrum baseline and truncate some expected band intervals. A specific interval 1500–1800 cm^{-1} was observed as represent the covalent bond of amide I band [27, 37]. The Raman signals were then convoluted and fitted into sub-peaks using Origin 2019b software (OriginLab Corporation, USA), especially to calculate the percentage areas of ordered and disordered α -helix backbone of protein secondary structure in the amide I band [37]. The objectives were to confirm the effect of pre-heat at 70 $^{\circ}\text{C}$ for 1 h in denaturing the protein structures before used in tribocorrosion tests deliberately.

Figure 2b shows the testing electrolytes used in this study. Both as-FBS and de-FBS were diluted with DI water to 25% and 75% (v/v), or to a minimum of 17 g/L and 51 g/L total protein content, respectively. Analytical laboratory grade sodium chloride (NaCl) was purchased from Sigma, UK and used as-received salts ion in this study. The saline was then added to the FBS electrolytes to a concentration of 0.9% w/v NaCl. The 0.9% w/v NaCl without FBS (pure saline) was also used. FBS concentration was based on the version of ISO 14243–3 standard for hip simulation, which required a 25% (v/v) concentration of serum. The 75% (v/v) was aimed to be a comparative variable regarding the concentration

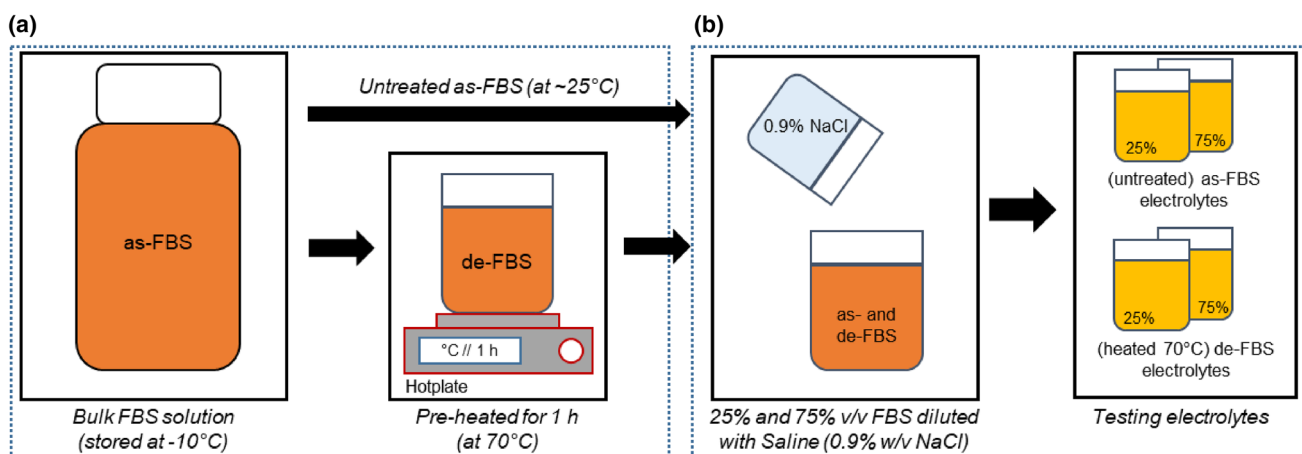


Fig. 2 Preparation of FBS-containing electrolyte: **a** pre-heating process at 70 $^{\circ}\text{C}$ for 1 h and **b** saline dilution for the FBS with different concentrations (25% and 75%)

effect [55, 57, 58]. In addition, the dilution process was conducted after the 1 h pre-heating process at 70 °C to avoid any concentration reduction and keep the FBS a similar condition with the untreated one.

2.3 Tribocorrosion Tests

A reciprocating tribometer (BICERI, UK) was employed to simulate tribocorrosion. The tribocorrosion test configuration involved a reciprocating alumina (Al_2O_3) ceramic ball, with $\text{Ø} = 12$ mm and grading standard of 25 (Atlas Ball and Bearing Company, UK), which directly in contact with a flat CoCrMo sample (exposed surface area = 3.80 cm^2). The initial mean Hertzian contact pressure ' P_{mean} ' was 565 MPa and achieved through the application of a constant normal load of 10 N [59]. The applied contact pressure was aimed to simulate an extreme movement of the hip joint, therefore, higher than in normal standard gait condition [55]. All tests were conducted with a 10 mm stroke length, 1 Hz frequency and sliding speed of 20 mm/s (1 cycle is equal to 1 s in tribocorrosion test), at room temperature 25 °C and equilibrium conditions (i.e. corrosion not forced). Total sliding time was varied between 3, 6 & 9 h. All tests were conducted in triplicate ($n = 3$). All samples had a rapid rinse with DI water, dried by compressed air and stored in a desiccator to avoid contamination before surface chemical analysis.

The reciprocating pin-on-plate tribometer was instrumented with a 3-electrode electrochemical cell controlled via a PGSTAT101 potentiostat (Metrohm Autolab, Netherlands), shown in Fig. 3. The electrochemical cell consists of the CoCrMo sample as working electrode (WE), a silver/silver chloride (Ag/AgCl) reference electrode (RE) and platinum (Pt) disc counter electrode (CE), respectively.

2.3.1 Electrochemical Measurements

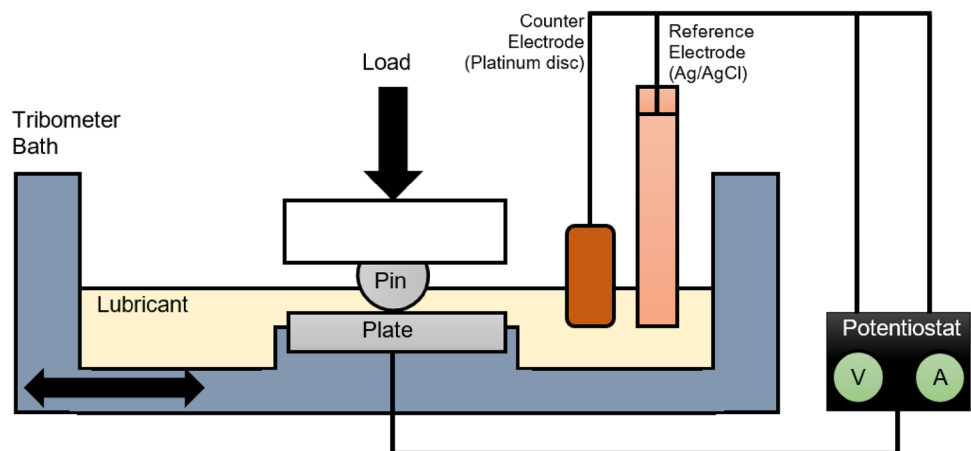
Corrosion and tribocorrosion were measured through a combination of Open Circuit Potential (OCP) and intermittent

Linear Polarization Resistance (LPR) measurements. OCP was measured by recording the potential difference between the WE and RE electrode at a rate of 1 Hz. There is no current flowing between the CE and WE as the anodic and cathodic reactions of the CoCrMo sample are in equilibrium. The evolution of OCP during the test can give a semi-quantitative assessment of the system's corrosion.

Intermittent LPR measurements were taken at 500 s after immersion, at 1.5 h intervals during the sliding and 500 s after the test stopped to assess the materials resistance to polarization and subsequent corrosion current. To determine Polarization Resistance ' R_p ', the potential of the WE was shifted ± 10 mV versus OCP with a scan rate of 0.25 mV/s and the resultant current measured. The LPR technique is considered non-destructive because it operates within a few milli-volts (mV) of the sample OCP. LPR measurements were conducted intermittently to avoid any changes within the system which may arise from sustained application of an over-potential. ASTM G119-09 [60] and referenced document G59-97 [52] describe the use of the LPR technique and Stern-Geary coefficients to determine corrosion currents within tribocorrosion systems [60].

Figure 4 shows an example plot of current vs potential obtained from an LPR test under (a) static and (b) sliding conditions (the example tested in saline). A linear E-I response around zero net current was observed. The slope of measured current as a function of applied potential represents the R_p which was calculated using the voltage window of ± 5 mV around zero net current as utilized in the previous studies [8, 61]. The obtained R_p was converted into a corrosion current density ' I_{corr} ' (Ampere) using the Stern-Geary formula (Eq. 1) and a standard set value of Tafel constants (β_a and $\beta_c = 120$ mV/decade) obtained through an extrapolation process of the Tafel plot. The I_{corr} was integrated over the tribocorrosion test time ' t ' (second) to obtain the total charge transfer of ions removal, ' Q ' (Coulomb) in Eq. 2, which passed through a substance [61].

Fig. 3 Instrumented reciprocating tribometer scheme (this image is reproduced from the previous study [8])



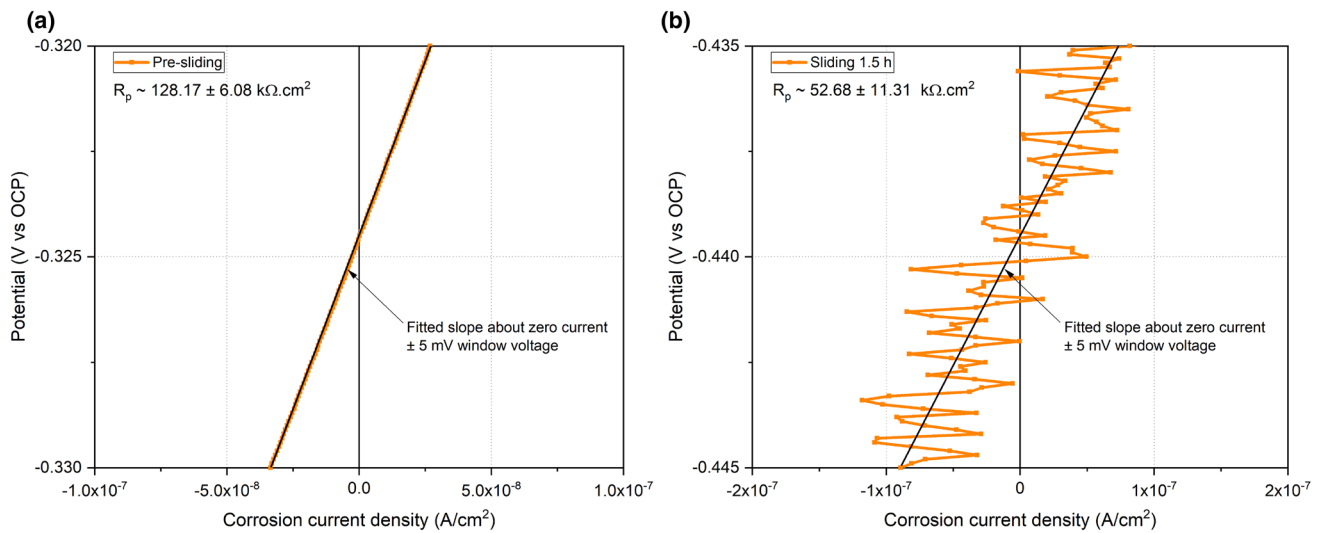


Fig. 4 Example of polarizations during LPR scan at a static and b sliding conditions in 0.9% saline solution

$$I_{corr} = \frac{\beta_a \cdot \beta_c}{2.303(\beta_a + \beta_c)} \cdot \frac{1}{R_p} \tag{1}$$

$$Q = \int_0^t I_{corr} dt \tag{2}$$

After obtaining the charge transfer from LPR data, Faraday’s Law was used to estimate a mass loss ‘m’ of metallic surface resulted from corrosion components as in Eq. 3. Faraday’s constant ‘F’ was 96,500 C/mol and molar mass ‘M’ was 55.7 g/mol, obtained from the stoichiometric average of CoCrMo alloys composition. Therefore, the valence number ‘n’ was 2.4 and density ρ was 8.29 g/cm³. These values were also similar to those used in previous studies with CoCrMo sample [61–63]. The estimated mass loss was divided by the value of material density, as in Eq. 4, to calculate the volume loss due to corrosion ‘V_c’.

$$m = \frac{M \cdot Q}{n \cdot F} \tag{3}$$

$$V_c = \frac{m}{\rho} \tag{4}$$

2.4 Post-Test Wear Analysis

Surface analysis was conducted to examine the influence of protein configuration on CoCrMo surfaces subjected to tribocorrosion. The methodologies used are described herein:

2.4.1 Chemical Analysis

An EVO MA 15 (Carl Zeiss, Germany) Scanning Electron Microscopy (SEM) was used to observe the worn surface morphology and film depositions at the surface. Energy Dispersive X-ray Spectroscopy (EDS) enabled the observation of the chemical elements on the sample surface. EDS captured the mapping scans of common elements with accelerating voltage of 10 kV. Atomic quantitative analysis was taken from two spots inside the wear scar in each sample (n = 3) by EDS. Previous studies [8, 64] characterized that typical elements, e.g. carbon, nitrogen, sulfur, oxygen and metallic traces, were found on the retrieved implant surface.

2.4.2 Atomic Force Microscopy (AFM)

AFM (Bruker, MA, USA) was employed to observe the high resolution of topography images of deposited films with the CoCrMo wear scars. AFM was used in tapping mode (in air) to generate mapping inside wear scar after tested in all electrolytes. Image processing and data acquisition were conducted by NanoScope Analysis software (Bruker, MA, USA) to obtain a high resolution of topography. The scans were taken on an area of 5 × 5 μm at different spots (n = 3).

2.4.3 Vertical Scanning Interferometry (VSI)

VSI (NPFlex, Bruker, USA) was used to obtain sample surface profiles as three-dimensional representation and measure the total volume loss after 3 h, 6 h and 9 h sliding. VSI used white light and surface reflection to generate fringes with a magnification lens of 10x. The results were proceeded by the Vision64 software (Bruker, MA, USA) to generate

three-dimensional images. Wear scar contour and negative volume were calculated after removal of surface form and tilts. The total volume loss was measured by adjusting the layer height to calculate all points below the plane.

Specific wear rates then were calculated via Archard's Law [65, 66]. Equation 5 [67] shows that the specific wear rate 'SWR' ($\mu\text{m}^3/\text{N.m}$) can be calculated using total volume loss ' V_{total} ' (μm^3) divided by constant normal load 'W' (N) and sliding run distance ' ΔS ' (216 m, 432 m and 648 m for 3 h, 6 h and 9 h sliding, respectively). SWRs were calculated for each tribocorrosion test interval as an indication of changes in the degradation mechanism.

$$V_{\text{total}} = \text{SWR} \cdot W \cdot \Delta S \quad (5)$$

2.5 Tribocorrosion Mechanistic Approach

The dominant degradation mechanism, either electrochemical corrosion or mechanical wear processes, can be estimated using a mechanistic approach by Uhlig's formula (Eq. 6) [68]. Based on the studies by Stack et al. [69, 70], the total volume loss (V_{total}) can be categorized into volume loss due to electrochemical corrosion (V_C) and volume loss due to mechanical wear (V_W). Since the V_{total} has been measured by VSI and the V_C was estimated via Faraday's Law, V_W can be calculated via subtraction.

$$V_{\text{total}} = V_W + V_C \quad (6)$$

The mechanisms of tribocorrosion can be determined by the ratio between V_C over V_W [69, 70]. The following criteria was used to identify the dominating tribocorrosion mechanisms:

$$\text{Wear} : V_C/V_W \leq 0.1$$

$$\text{Wear - corrosion} : 0.1 < V_C/V_W \leq 1$$

$$\text{Corrosion - wear} : 1 < V_C/V_W \leq 10$$

$$\text{Corrosion} : V_C/V_W > 10$$

2.6 Statistical Analysis

All results are presented as an average attributed with error bar (standard deviation / SD). Statistical analysis was conducted using one-way analysis of variance (ANOVA). The number of the tested samples (n) were categorized into specific variables (e.g. electrolyte and test duration) as comparative groups. ANOVA test can determine significance of the electrolytes effect on tribocorrosive degradation of CoCrMo surface. The level of significance used $\alpha=0.05$

to be compared with a p -value in all mentioned comparison. The compared results that are significantly different ($p < 0.05$), have been marked by an asterisk (*).

3 Results

3.1 Raman Confirmation

Figure 5 shows the Raman spectra for FBS before (as-FBS) and after heat treatment (de-FBS). A significant decrease in the amide I peak intensity was seen for de-FBS after subjected to heat treatment at 70 °C for 1 h. The deconvoluted area percentage of ordered α -helix decreased with the application of heat treatment and enhanced the disordered α -helix percentage within the amide I band, indicating the native structure became denatured.

Characterization of the changes in pre-heated FBS at 70 °C for 1 h was conducted in this study via Raman analysis. A change in the amide I peak intensity, showing the decrease in ordered α -helix and an increase in disordered α -helix deconvoluted area percentages, was seen for de-FBS after thermally treated 70 °C for 1 h. A past study [37] demonstrated that the protein conformational structure is reversible at temperatures below 50 °C. However, protein becomes irreversibly unfolded after passing the heat treatment higher than 60 °C. After reaching 70 °C, the proteins can be altered in their physical form into a gel-like structure along with a change in colour. That study also showed that range of the critical temperature for protein denaturing was within 50–60 °C. Similar to this study, the unfolding processes (α -helices secondary structure) were indicated by the shifting of Raman peaks and a reduction in signal intensity. Therefore, protein structure in de-FBS electrolyte used in this study was suggested to be fully denatured since the pre-heating (at 70 °C for 1 h) treatment has passed the unfolding critical temperature.

3.2 OCP Measurements

Figure 6a and b show the transient OCP evolution during early immersion (pre-sliding), tribocorrosion test and after the test (post-sliding) in all electrolytes. Upon immersion, the OCP of all tests was seen to increase likely due to the hydration of the surface oxide layer. A typical de-/re-passivation behaviour upon the start of sliding was seen for all samples [71]. After sliding, the OCP in all electrolytes recovered to values greater than those recorded in the initial static immersion stage.

In the static immersion stage (pre-sliding), the CoCrMo sample in saline electrolyte had a more positive OCP value when compared to 75% FBS-containing electrolytes and 25% de-FBS. During this test stage, the OCP for 25%

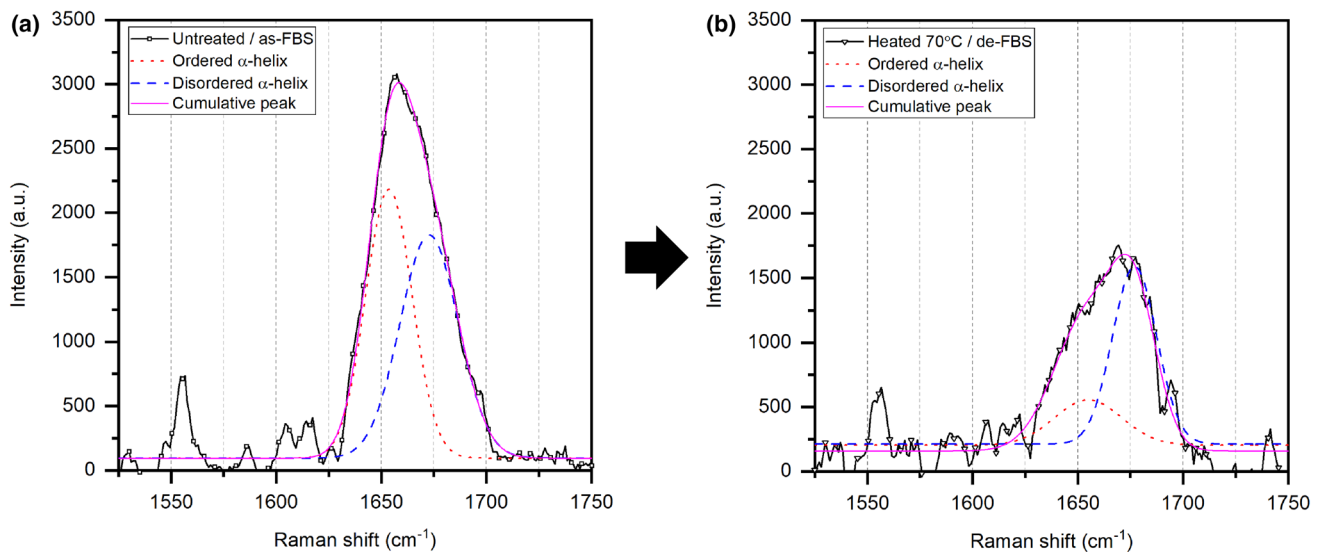


Fig. 5 Deconvolution samples of the amide I Raman band to fit sub-peaks of α -helix structure for **a** the untreated / as-FBS and **b** after 1 h heated at 70 °C / de-FBS

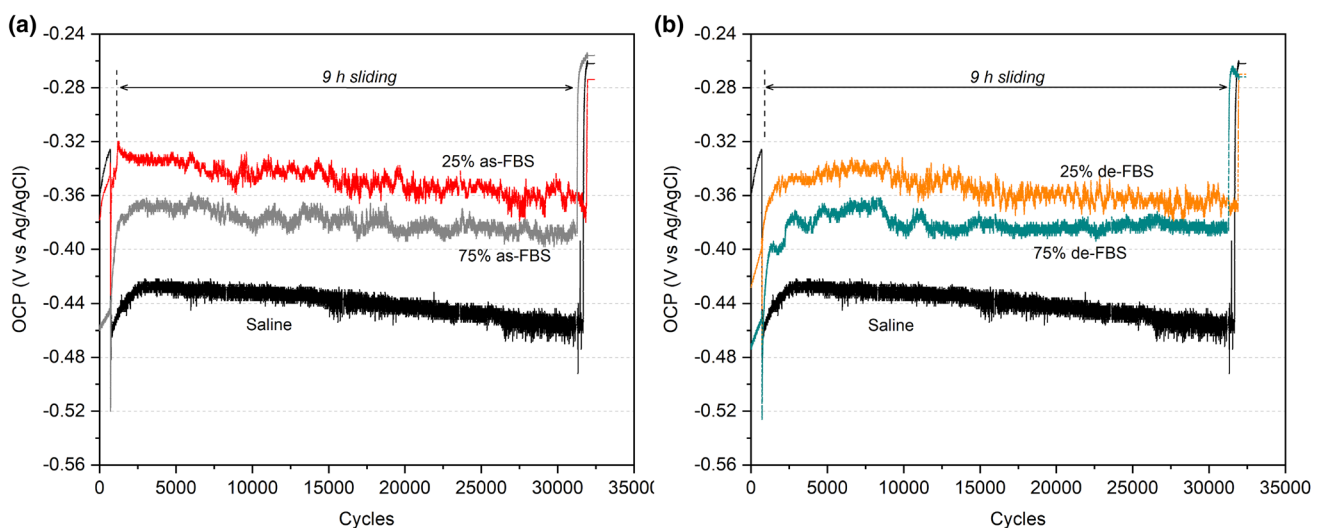


Fig. 6 The evolution of transient OCP in **a** as-FBS and **b** de-FBS measured over early immersion (pre-sliding), tribocorrosion test and after test stopped (post-sliding) to compare saline and different FBS concentration

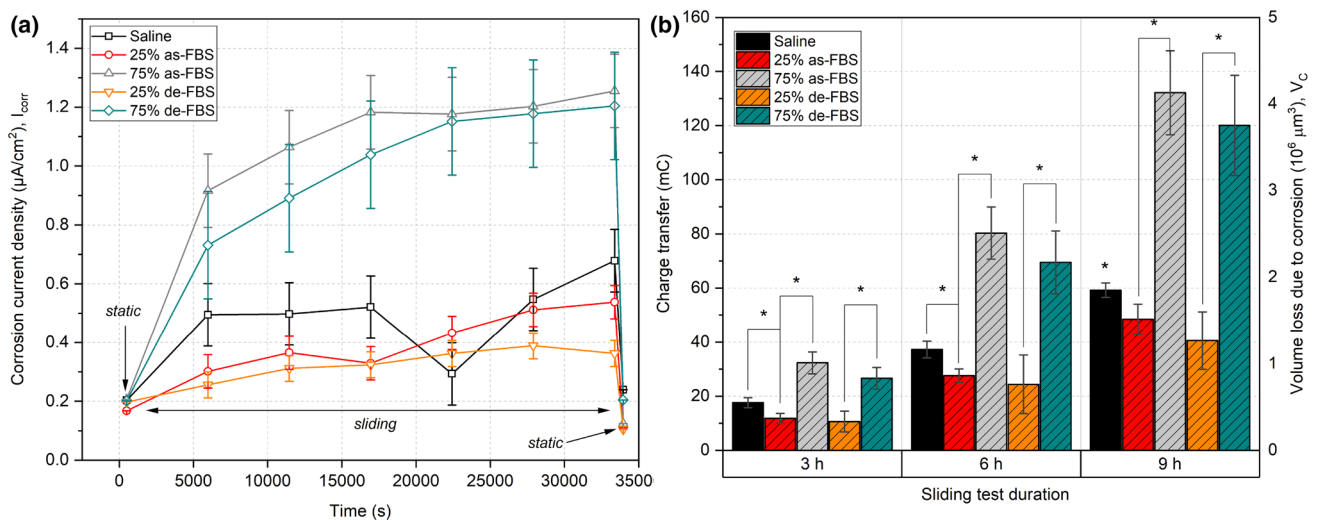
de-FBS was seen to be more positive when compared to sample immersed in 75% de-FBS. During sliding, the transient OCP in saline was more negative when compared to all FBS electrolytes. Similar to the pre-sliding stage, the transient OCP for 25% de-FBS during sliding stage was seen to be more positive when compared to sample slid in 75% de-FBS. In post-sliding stage, all electrolytes had a more positive transient OCP value when compared to their pre-sliding stage. Furthermore, 75% as-FBS had a more positive OCP when compared to 25% de-FBS sample.

3.3 Volume Loss Due to Corrosion

Table 1 shows the average values and standard deviations of the polarization resistance (R_p) calculated from LPR measurements before, during and after sliding stages. Figure 7a shows the evolution of corrosion current density (I_{corr}) derived from the application of Stern-Geary formula (Eq. 1) using the value of R_p at each points of the LPR measurements during the tribocorrosion tests. All samples tended to have a lower current density in the absence of

Table 1 The average R_p values calculated from the LPR measurements during tribocorrosion tests

Conditions	Time (Seconds)	Polarization resistance (R_p), $k\Omega \cdot \text{cm}^{-2}$				
		Saline	25% as-FBS	75% as-FBS	25% de-FBS	75% de-FBS
Static	500	128.17 ± 6.08	155.58 ± 14.39	126.02 ± 13.59	131.93 ± 16.72	129.06 ± 4.60
Sliding	5980	52.68 ± 11.31	86.44 ± 16.26	28.43 ± 3.87	101.90 ± 17.58	35.64 ± 8.89
	11,460	52.36 ± 11.17	71.40 ± 11.09	24.48 ± 2.87	83.63 ± 11.84	29.25 ± 5.99
	16,940	50.04 ± 10.20	79.12 ± 13.62	22.02 ± 2.32	80.46 ± 10.96	25.08 ± 4.41
	22,420	88.85 ± 32.17	60.22 ± 7.89	22.15 ± 2.35	71.90 ± 8.76	22.63 ± 3.58
	27,900	47.63 ± 9.24	50.93 ± 5.64	21.67 ± 2.46	67.03 ± 7.61	22.12 ± 3.43
33,380	38.39 ± 6.01	48.44 ± 5.10	20.76 ± 2.06	71.90 ± 8.87	21.64 ± 3.28	
Static	33,960	109.15 ± 4.35	237.23 ± 33.46	210.48 ± 37.90	249.72 ± 39.90	127.39 ± 4.55

**Fig. 7** **a** The evolution of corrosion current density measured during 9 h tribocorrosion and **b** comparison of total charge transfer and V_C with a split of test durations ($n=3$; SD bar; $*p < 0.05$)

sliding, both before and after sliding when compared to sliding stage. Furthermore, the current densities tended to gradually increase as a function of time during the sliding stage. Overall for all tests conducted in 25% FBS-containing electrolytes the current densities were lower than tests conducted in 75% FBS and saline electrolytes. In sliding, de-FBS tended to result in lower current densities when compared to the as-FBS electrolytes.

Figure 7b shows the average total charge transfer for all tribocorrosion tests. For all test durations, the use of 25% FBS and 75% FBS was seen to significantly decrease and increase the total charge transfer, respectively, when compared to saline. Furthermore, an increase of charge transfer was observed for all 75% FBS-containing electrolytes when compared to all samples slid in 25% FBS-containing electrolytes. No significant difference in total charge transfer was observed between CoCrMo tested in as-FBS and de-FBS.

3.4 Chemical Analysis

Figures 8 and 9 show SEM and EDS analysis of the wear scars (two different spots) for CoCrMo surfaces after slid for 9 h in as-FBS and de-FBS electrolytes, respectively. These SEM images were supported with EDS mapping to observe the distribution of elements within the wear scar. Several species, i.e. carbon (C) and sulphur (S), were made an appearance along with metal elements (Co, Cr and Mo) and oxygen (O). EDS analysis at wear scar edges and corner indicated signs of carbon and oxygen. Sulphur and traces of carbon were also observed within the wear scar. The darker layers dominated the tip corner of wear and the inside wear track and along the wear borders. The EDS confirmed carbon and sulphur from bovine serum and also oxide from the passive reformation. Wear scar at 25% FBS showed a smaller width (via SEM image scale) and more oxide films were seen more at the corner when compared to 75% FBS.

Fig. 8 SEM/EDS in the wear scar of CoCrMo alloys after tested in **a** 25% as-FBS and **b** 75% as-FBS

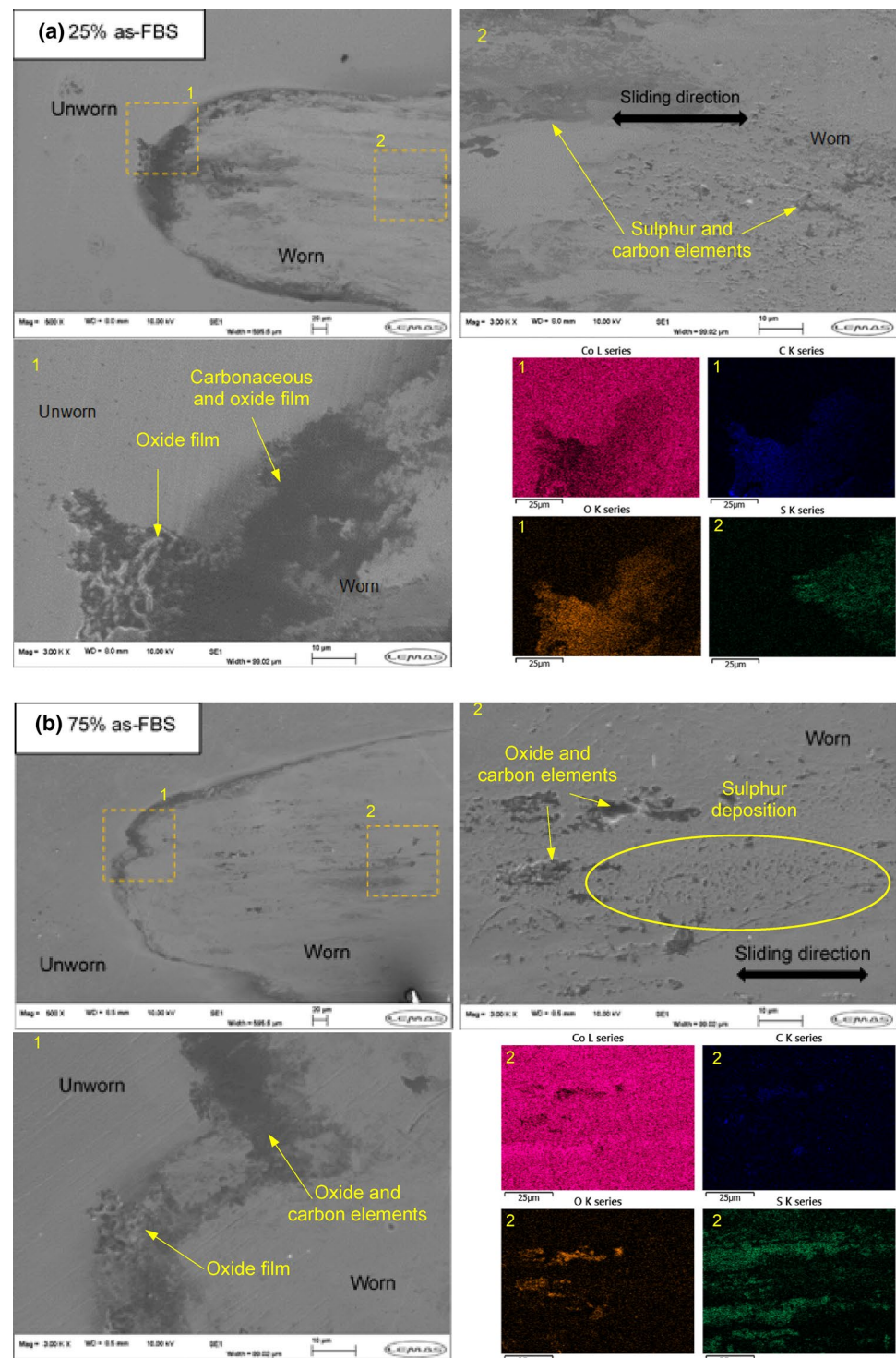
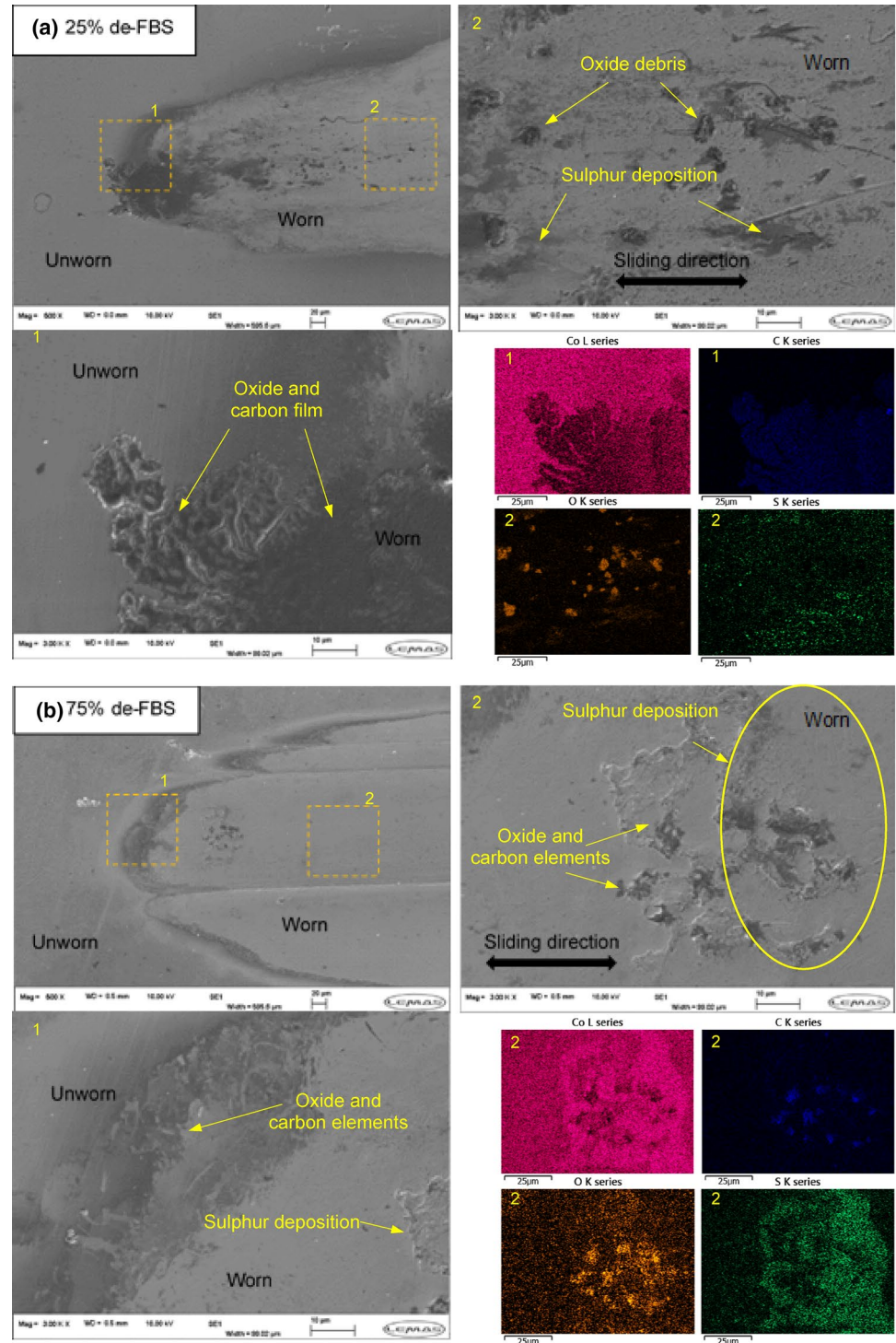


Table 2 shows the average atomic percentages of elements ($n = \text{two different spots}$) found on CoCrMo surfaces after 9 h tribocorrosion test. The atomic percentage of carbon, oxygen and nitrogen were relatively lower on surfaces slid in 75% FBS samples when compared to 25% FBS samples. On the contrary, the sulphur element

percentage was higher on 25% FBS samples when compared to 75% FBS samples. Carbon and oxygen were found to increase in the wear scar of denatured FBS samples. The sulphur was observed to be higher on samples slid in 75% FBS-containing electrolytes when compared to 25% FBS electrolytes.

Fig. 9 SEM/EDS in the wear scar of CoCrMo alloys after tested in **a** 25% de-FBS and **b** 75% de-FBS



3.5 Surface Topography

Figure 10 shows representative images of the surface topography of samples slid in the different electrolytes, as measured by AFM. Signs of abrasion (characterized by grooves/scratches) was observed in the wear scar of the CoCrMo samples slid in a saline electrolyte. AFM analysis

of CoCrMo surfaces slid in FBS electrolytes displayed evidence of film formation and localized build-up arranged in the direction of sliding. CoCrMo surfaces slid in as-FBS showed a smoother texture compared to those slid in de-FBS. The film deposition for CoCrMo surface slid in de-FBS was seen to be more scattered when compared to surfaces slid in as-FBS. Samples slid in de-FBS demonstrated an

Table 2 EDS atomic percentage of deposited elements at CoCrMo surfaces tested in saline and FBS-containing electrolytes ($n=2; \pm$ SD)

Elements	Atomic percentages (at%)				
	Saline	25% as-FBS	75% as-FBS	25% de-FBS	75% de-FBS
Co	50.19 ± 0.95	41.11 ± 0.91	43.76 ± 0.47	29.91 ± 0.96	44.03 ± 0.39
Cr	18.72 ± 0.48	12.80 ± 0.20	11.99 ± 0.49	8.99 ± 0.23	10.29 ± 0.53
Mo	3.36 ± 0.16	6.58 ± 0.07	6.89 ± 0.08	5.02 ± 0.11	7.02 ± 0.08
O	27.73 ± 0.83	13.52 ± 0.95	8.51 ± 0.25	25.64 ± 0.60	9.46 ± 0.06
C	–	19.71 ± 0.74	15.53 ± 0.23	24.29 ± 1.09	19.26 ± 0.25
N	–	2.17 ± 0.07	1.82 ± 0.05	2.67 ± 0.11	1.20 ± 0.02
S	–	4.13 ± 0.58	11.52 ± 0.16	3.50 ± 0.47	8.75 ± 0.83

increased amount of localized build-up of material on the surface when compared to surfaces slid in as-FBS.

3.6 Total Volume Loss

Figure 11a shows the V_{total} measured by VSI with respect to tribocorrosion test duration in all electrolytes. V_{total} was significantly higher for CoCrMo slid in saline when compared to all FBS electrolytes for all test durations. After 3 h sliding tests, the V_{total} was higher for all 75% FBS-containing electrolytes when compared to 25% FBS-containing electrolytes. CoCrMo tested in 75% de-FBS was observed to significantly decrease the V_{total} when compared to 75% as-FBS, indicating the role of denaturing protein in FBS. No significant difference was observed between all FBS electrolytes after the 6 h sliding tests. Furthermore, after the 9 h sliding tests the V_{total} for 25% de-FBS was significantly lower when compared to CoCrMo slid in 25% as-FBS and 75% de-FBS.

Figure 11b shows the SWRs for each time durations of the tribocorrosion test. The purpose of the SWR comparison was to interrogate any degradation mechanism change within each test interval (every three hours during the 9 h tribocorrosion test). During 3 h sliding tests, the SWR was suggested to change due to protein concentration in FBS, showing higher average SWR for all 75% FBS-containing electrolytes when compared to 25% FBS-containing electrolytes. Furthermore, CoCrMo tested in 75% de-FBS was observed to significantly decrease SWR when compared to 75% as-FBS, indicating the role of denaturing protein in FBS. No significant difference was observed between FBS electrolytes during 6 h sliding tests. After 9 h of sliding test, the SWR for 25% de-FBS was seen to be significantly lower when compared to CoCrMo slid in 25% as-FBS and 75% de-FBS.

3.7 Volume Losses due to Tribocorrosion

Figure 12 shows the contribution of volume loss due to corrosive (V_C) and mechanical (V_W) processes to the total tribocorrosive volume loss (V_{total}) as a function of test duration and electrolyte. The V_C was estimated using Faraday's Law

(refer to Fig. 7b), allowing the subtraction of V_{total} to obtain V_W . For all test durations, saline had the highest V_W when compared with all FBS-containing electrolytes. Following a 3 h sliding test, the V_W for 25% as-FBS and 75% de-FBS were significantly lower when compared to 75% as-FBS. After 6 h sliding tests, a significant difference in V_W was observed for 25% de-FBS, which was higher when compared to 75% de-FBS. After 9 h sliding tests, CoCrMo slid in 25% as-FBS was seen to have a significantly higher V_W when compared to 75% as-FBS and 25% de-FBS. Furthermore, the V_W for 25% de-FBS was significantly higher when compared to 75% de-FBS.

Figure 13 shows the volume loss ratio (%-contribution) as a function of the test duration and electrolyte. In all cases, the %- V_W was seen to contribute to more than 70% of the V_{total} . In the case of CoCrMo slid in 75% de-FBS, the %- V_C was seen to increase with increased sliding time, accounting for ~ 30% of the total material loss. This trend is hypothesized to be influenced by a change in tribochemistry behaviour on the CoCrMo surface as a function of the sliding duration and different protein concentrations in FBS electrolytes. FBS with a 75% concentration is hypothesized to form a tribofilm on the CoCrMo surface over the sliding cycles, improving the lubricity to minimize the incremental rate of mechanical wear degradation based on the results of this study. However, this particular concentration of protein in electrolyte increased the rate of corrosion. There was no evidence of the effect of protein structure on the incremental rate of volume loss contributors over all test durations.

To investigate the link between protein structure and concentration effects, the V_C and V_W can be used to indicate tribocorrosion behaviour via the mechanistic approach [72] after 3, 6 and 9 h sliding tests in various FBS-containing electrolytes (Fig. 14). The tribocorrosion process on CoCrMo slid in saline was constantly dominated by the mechanical wear mechanism during the 3, 6 and 9 h sliding tests. On the other hand, all of the FBS-containing electrolytes consistently showed that the wear-corrosion mechanism was dominating the tribocorrosion degradation for all sliding test durations, except for 25% de-FBS after 6 h sliding in, which represented a wear dominated regime.

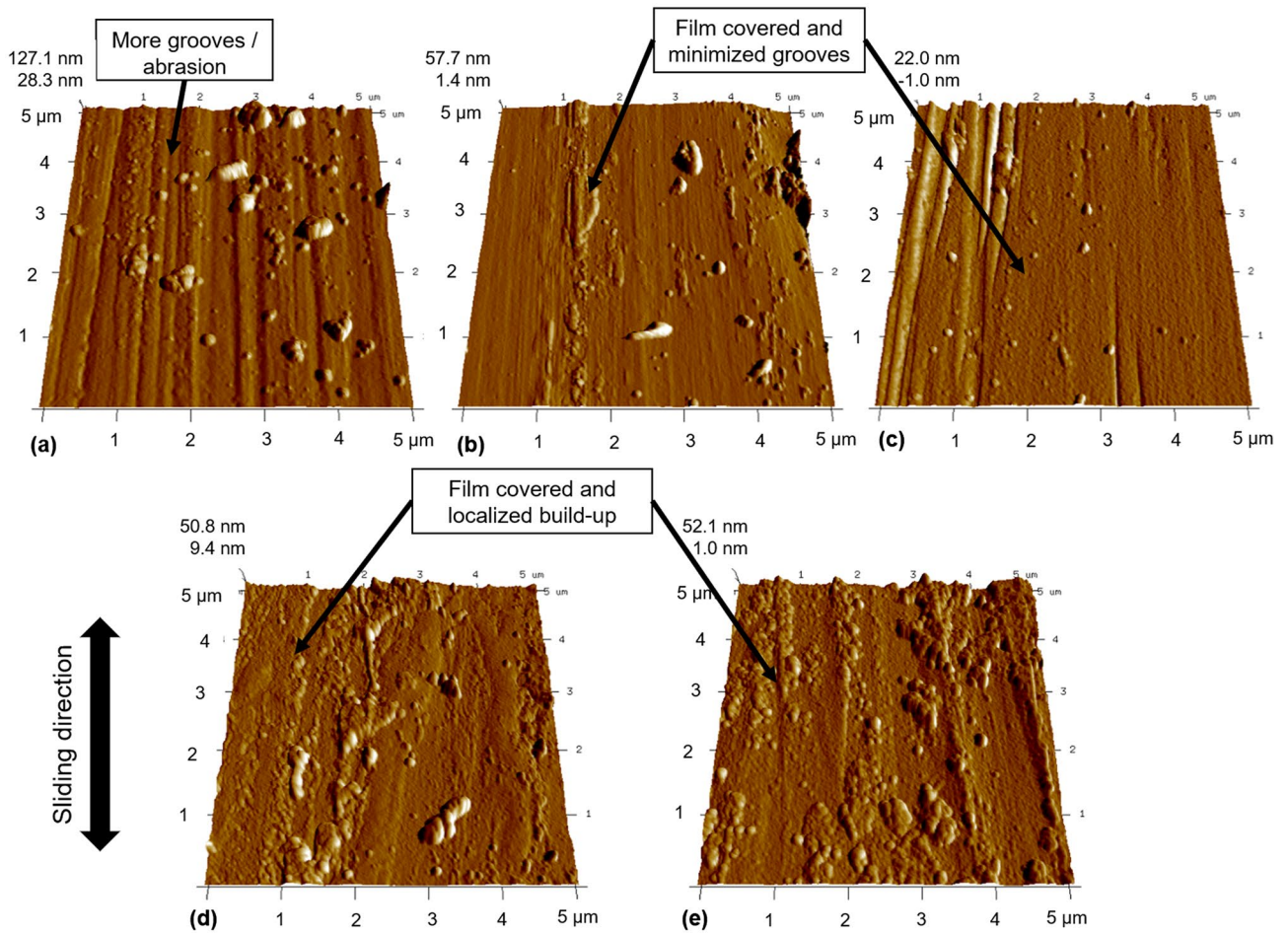


Fig. 10 AFM $5 \times 5 \mu\text{m}$ images of wear scar after tested in **a** saline, untreated **b** 25% FBS and **c** 75% FBS, as well as denatured **d** 25% FBS and **e** 75% FBS

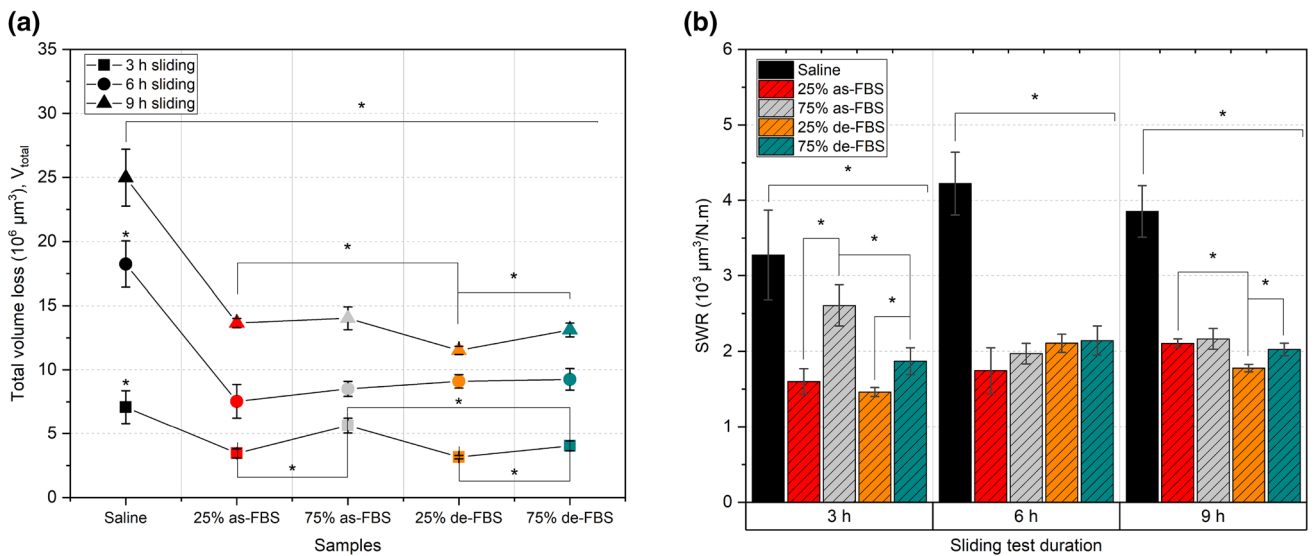


Fig. 11 Comparison **a** total volume loss measured by VSI and **b** SWR with a split of test durations of 3, 6 and 9 h tribocorrosion tests in all electrolytes ($n=3$; SD bar; $*p < 0.05$)

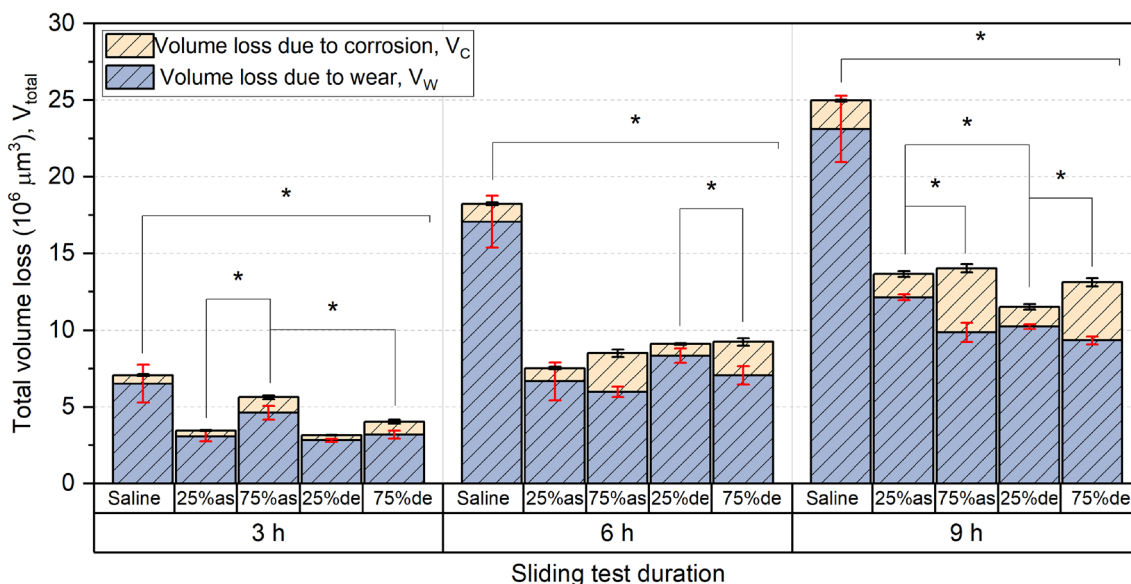


Fig. 12 The contributors to total volume loss as a function of the tribocorrosion test duration for all electrolytes ($n=3$; SD bar; $*p < 0.05$ for V_w as a function of electrolyte)

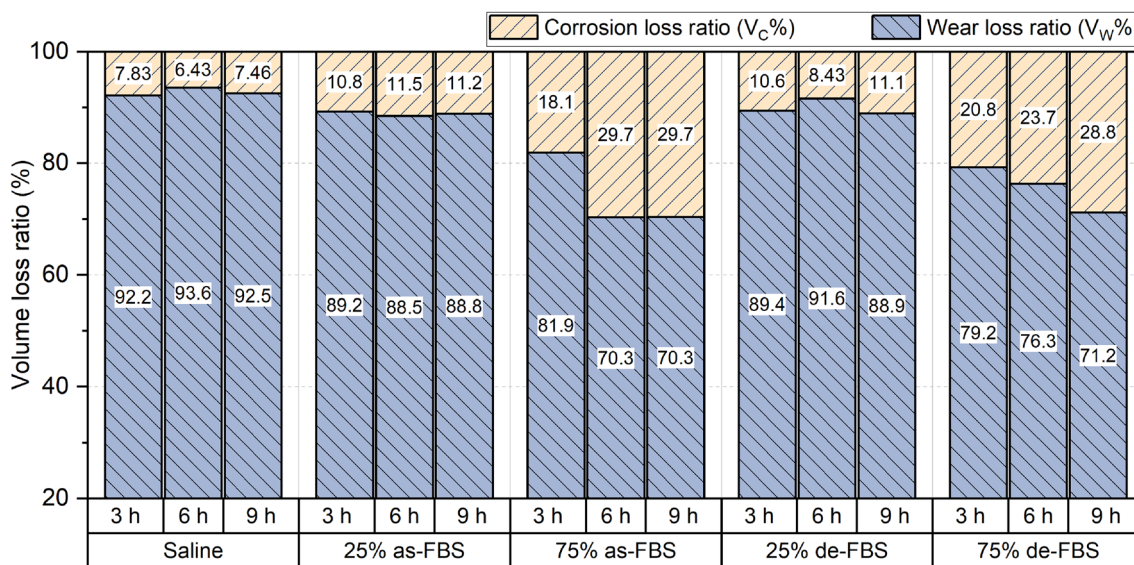


Fig. 13 The ratio of the contributing volume loss components as a function of tribocorrosion test duration for all electrolytes

However the total volume loss was not significantly different when compared to the 25% as-FBS in the wear-corrosion regime. Furthermore, the tribocorrosion mechanism was shifted back onto the wear-corrosion mechanism after 9 h sliding.

4 Discussions

Tribocorrosion of biomedical alloys remains of significant interest to the medical device community due to the potential to elicit adverse soft tissue reactions and associated with higher than acceptable revision rates. Whilst the basic tribocorrosion mechanisms of Co-based alloys have been established [2, 73], the roles of system variables on the tribocorrosion and tribochemical processes are still to

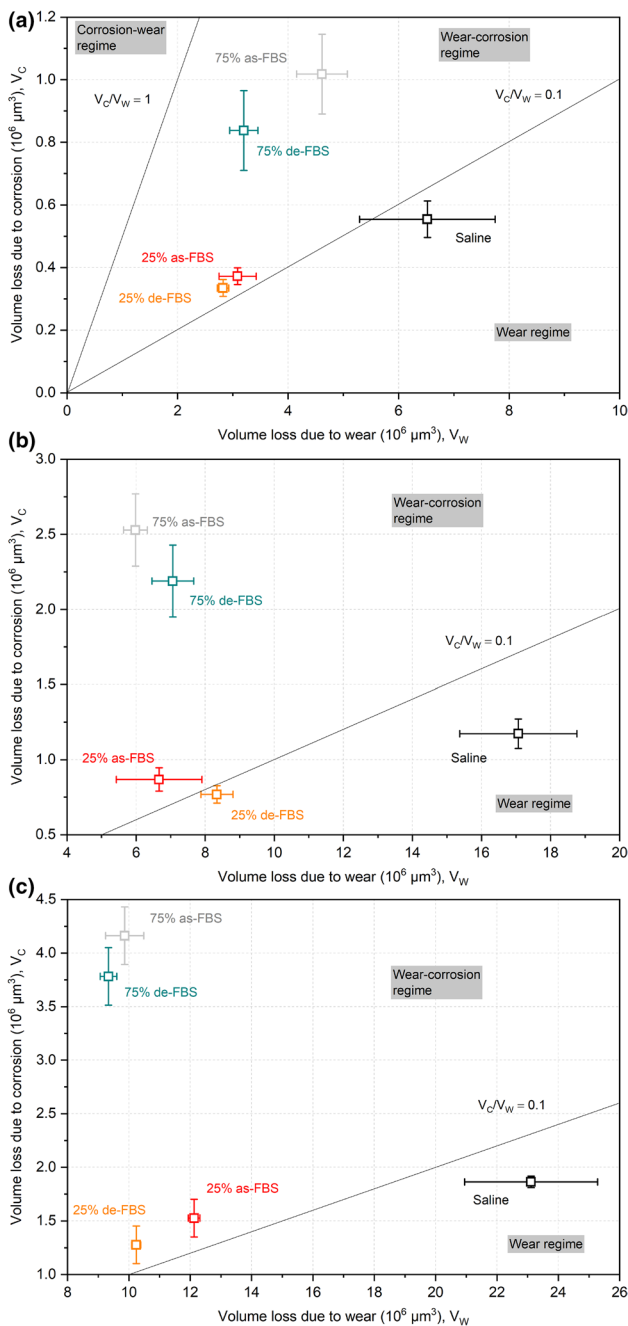


Fig. 14 The tribocorrosion behaviour of CoCrMo using a mechanistic approach after **a** 3 h, **b** 6 h and **c** 9 h sliding tests in all electrolytes ($n=3$; SD bar)

be fully elucidated. For the first time, tribocorrosion tests have been conducted in the pre-heated (at 70 °C for 1 h) FBS-containing electrolyte. This study aimed to understand the role of the protein structure and its concentration on the tribocorrosion and tribochemical processes occurring on of CoCrMo alloys. A preheating approach to denature proteins within the electrolyte prior to sliding was taken in an attempt to isolate the effects of increased

external temperature on corrosion kinetics. The major findings from this study indicate that the protein structure and concentration affects (1) the tribochemical processes occurring on CoCrMo surfaces and (2) the mechanisms of tribocorrosion material loss.

From Fig. 12, the denatured protein structure tends to reduce the volume losses owing to mechanical wear (V_w) when compared to as-received FBS-containing electrolyte. The de-FBS also incurred a lower total charge transfer which indicated a reduction in volume loss due to corrosion (V_c). The reason for this decreasing behaviour can be linked with the denaturing effect on protein–metal interaction and tribofilm deposition; tribofilm formation was more abundant on samples slid in denatured protein electrolytes (Fig. 10). This correlates with observations from Mishina and Kojima [74] who investigated the role of serum albumin on friction in the combinations of CoCrMo, polyethylene (UHMWPE) and alumina samples. The study showed that protein denaturation occurs in the temperature range of 50–55 °C, affecting the absorption behaviour and decreasing friction and wear. In this study, a higher EDS carbon signal was detected and evidence of tribofilm formation in the wear tracks of CoCrMo slid in de-FBS electrolytes was observed, complimenting the reduced material loss mechanism. This correlates with other studies that have shown carbonaceous tribofilm deposition can reduce the corrosion, wear and the lubricity of CoCrMo alloy in the tribological condition [75, 76]. Wimmer et al. [21, 77] further hypothesized that tribofilms (from retrieval and in vitro hip simulator) were formed after the denaturation process due to the mechanism of shear stress and flash temperatures at the contacting surfaces. In addition to the carbon observation, this study provides evidence of cobalt, molybdenum and sulphur on the surfaces after tribocorrosion (Table 2); the concentration of which is affected by the FBS concentration and protein structure. The presence of sulphur in the form of cobalt sulphide has been observed via XPS and SAED images within the tribofilm on the CoCrMo surface slid in bovine serum by Hesketh et al. [41]. Furthermore, the authors have identified Mo-S speciation via XPS in a previous study [8]. The presence of sulphur on the surface and its tendency to reduce volume loss due to mechanical wear have been demonstrated in several studies [78, 79]. Thermal heating and mechanical shear has been shown to modify the disulphide bridges in the protein structure along with amide I band [33, 43, 80]. It has been hypothesized by Maskiewicz et al. [29] that denatured protein in FBS promotes proteinaceous tribofilm formation due to higher kinetic adsorption rates, which tends to interact with metal ions, suppress the metal ions release and reduce material loss owing to mechanical wear [40, 56].

The higher FBS concentration was observed to increase the volume loss due to corrosion V_c . This behaviour indicates that a higher FBS concentration can enhance the

synergism between wear and corrosion during sliding. In line with the observations by Thornley et al. [81] it can be hypothesized that the increased FBS concentration will inhibit oxygen-reduction reactions and delay passive film formation, hence resulting in a higher/sustained dissolution process. The behaviour of protein aggregation had a higher protein concentration when compared to the lower concentration compliments observations made by Sun et al. [82], reporting the misfolded protein aggregates found on the worn CoCrMo surfaces with various dimensions. The proteins seemed to be aggregated and bonded with metal debris and ions, forming agglomeration bodies trapped within the contact surface. In this study, the aggregated proteins in high concentration coincided with increased corrosion loss (Fig. 7b). These proteins also tended to produce a typical abrasive mechanism, indicated in the AFM (Fig. 10) and SEM results (Figs. 8 and 9). The effect investigated by Sun et al. [83] also showed that the increasing protein concentration reduced CoCrMo resistance to polarization (and increase corrosion) due to competitive behaviour. The concentration also affected the potential at the CoCrMo surface in a static condition [44]. This behaviour is in strong agreement with a study by Vidal and Munoz [84] that characterized the electrochemical behaviour on CoCrMo alloys in simulated body fluid. Albumin has been shown to reduce the polarization resistance and inhibit the oxide film formation in a static test. The protein concentration accelerated the anodic reaction since the adsorbed protein can bind and transport the metal ions away from the electrolyte/metal interfaces. A wear-corrosion dominated mechanism in all FBS electrolytes was observed in this study. This mechanistic behaviour is in strong agreement with a study by Mathew et al. [2] who showed a wear-corrosion dominated degradation in a bovine calf serum electrolyte compared to a wear dominated mechanism in a saline electrolyte. This study further shows that a lower protein concentration (25% FBS, in this case) tends to shift the tribocorrosion system towards the wear regime by reducing V_C when compared to the 75% FBS electrolytes (Fig. 14). In addition, the denatured FBS tends to lower the material degradation by reducing both V_C and V_W without changing the V_C/V_W ratio when compared to as-FBS electrolytes. This study also demonstrates that the contribution of wear and corrosion to the total mass loss of CoCrMo are independent of sliding duration/distance. This raises questions concerning the suitability of Archard's wear law assumptions when assessing tribocorrosive material loss mechanisms.

4.1 Limitations of the Study

Whilst this study has successfully identified the role of protein structure on the tribocorrosion of CoCrMo there are number of limitation in this study that need to be considered.

The use of LPR techniques and Stern-Geary theory provides a convenient and non-destructive methodology to determine the tribocorrosion currents of materials close to equilibrium [85, 86]. It has been shown by many authors that the application of sustained over-potential affects both the material-protein interactions and tribocorrosion mass loss mechanisms [38, 48, 87–89]. Furthermore, the approach has been used widely used in literature for a variety of tribocorrosion systems and is described in ASTM G119-09 [55, 90–93]. However the use of LPR techniques for tribocorrosion systems brings the following assumptions and limitations [94, 95]: Assumption of single charge transfer controlled reactions whereby the OCP is considered to be at 'equilibrium' and far removed from the reversible potentials (E_{rev}) of the anodic and cathodic reactions ($E_{revCo(II)/Co} \sim -519$ mV and $E_{revCr(II)/Cr} \sim -1155$ mV, according to mixed potential theory that is applied to interpret the potentials during rubbing on CoCrMo alloy in acidic buffered solutions [96]); in this case reversible potentials are for cathodic deposition of metals and anodic oxidation of species involved in reduction reactions which would result in a deviation from the approximately linear observations. Whilst the results from this study show the tribocorrosion system to be transient over the test duration, during abrasion the OCP measured continuously prior to LPR measurement can be considered stable with deviations in OCP < 3 mV/min [97] observed prior to polarisation (see supplementary data). Furthermore, no metal deposition was observed on CE surfaces and data presented in supplementary data show linear E-I indicating the tribocorrosion reactions are sufficiently far away from the reversible reactions and any possible capacitive charging effects have been mitigated through a sufficiently low voltage scan rate [98, 99]. Finally, based on the transient nature of the tribocorrosion system and formation of surface films that may limit the activation controlled corrosion reactions it is reasonable for the Tafel and proportionality constants to vary with time. Whilst we have assumed a constant 120 mV/dec, in practice a variation in β_a and β_c could result in a max error of 20% in stated corrosion currents. Future work to determine how these vary as a function of test duration and environment will be undertaken using a.c. techniques.

5 Conclusions

The effect of denaturing of FBS (via heat treatment) with different concentrations on tribocorrosion and tribochemistry on a CoCrMo alloy surface was successfully investigated. The following points are drawn from the obtained results as conclusions:

- The increasing protein concentration of FBS electrolytes was seen to reduce the transient OCP and promote

charge transfer significantly. However, de-FBS was seen to decrease the corrosion current density when compared to as-FBS electrolytes during sliding.

- The film depositions were seen on the de-FBS samples by AFM without confirming that those were protein species. A bigger localized build-up width, measured from 0.2–0.5 μm , was observed for de-FBS via AFM compared to as-FBS.
- SEM/EDS mapping scans observed higher carbon percentages at the wear scar of the de-FBS samples when compared to the as-FBS at both concentrations. An increase in sulphur elements was traced for both samples with a concentration of 75% FBS.
- The effects of protein structure and concentration in FBS electrolytes on the tribocorrosive degradation of CoCrMo surface is time-dependent during the tribological condition.
- The denatured protein in the FBS electrolyte can reduce the volume loss due to the corrosion and wear processes of the CoCrMo surface after being slid for 9 h.
- A higher protein concentration is indicated to have a positive effect in reducing the volume loss owing to mechanical wear after 6 h and 9 h sliding tests.
- However, the 75% FBS concentration instead increases the volume loss due to corrosion when compared to the 25% FBS concentration. It is hypothesized that the effect of protein content on volume loss due to corrosion is dependent on its concentration in electrolyte.

The future studies may need to study in vivo using a hip simulator to replicate more accurately the real articulating joint circumstances with more controlled parameters. The resistivity and thickness of the film formed, both passive oxide and adsorbed proteins, also clearly need to be further investigated as the function of protein structure and concentration. Those suggestions may contribute to a deeper understanding of protein-metal implant interactions in tribocorrosion mechanisms.

Supplementary Information The online version contains supplementary material available at <https://doi.org/10.1007/s40735-021-00585-6>.

Acknowledgements The authors wish to thank Dr. Chun Wang (University of Leeds) for the contribution in Raman spectroscopy and AFM tutorial sessions. The first author study received funding from the LPDP (Indonesia Endowment Fund for Education).

Declarations

Conflict of interest The authors have no conflicts of interest to disclose.

Open Access This article is licensed under a Creative Commons Attribution 4.0 International License, which permits use, sharing, adaptation, distribution and reproduction in any medium or format, as long

as you give appropriate credit to the original author(s) and the source, provide a link to the Creative Commons licence, and indicate if changes were made. The images or other third party material in this article are included in the article's Creative Commons licence, unless indicated otherwise in a credit line to the material. If material is not included in the article's Creative Commons licence and your intended use is not permitted by statutory regulation or exceeds the permitted use, you will need to obtain permission directly from the copyright holder. To view a copy of this licence, visit <http://creativecommons.org/licenses/by/4.0/>.

References

1. Liao Y et al (2013) CoCrMo metal-on-metal hip replacements. *Phys Chem Chem Phys* 15(3):746–756. <https://doi.org/10.1039/c2cp42968c>
2. Mathew MT et al (2011) Tribocorrosion behavior of CoCrMo alloy for hip prosthesis as a function of loads: a comparison between two testing systems. *Wear* 271(9):1210–1219
3. Drummond J, Tran P, Fary C (2015) Metal-on-metal hip arthroplasty: a review of adverse reactions and patient management. *J Funct Biomater* 6(3):486–499
4. Mathew MT et al (2010) Tribocorrosion behaviour of TiCxOy thin films in bio-fluids. *Electrochim Acta* 56(2):929–937
5. Yan Y et al (2013) Real-time corrosion measurements to assess biotribocorrosion mechanisms with a hip simulator. *Tribol Int* 63:115–122
6. Hallab NJ et al (2004) Differences in the fretting corrosion of metal-metal and ceramic-metal modular junctions of total hip replacements. *J Orthop Res* 22(2):250–259
7. Smith AJ et al (2012) Failure rates of metal-on-metal hip resurfacings: analysis of data from the national joint registry for england and wales. *The Lancet* 380(9855):1759–1766
8. Taufiqurrakhman M, Bryant M, Neville A (2019) Tribofilms on CoCrMo alloys: Understanding the role of the lubricant. *Biotribology* 2019:100101
9. Dumbleton JH, Manley MT (2005) Metal-on-Metal total hip replacement: what does the literature say? *J Arthroplasty* 20(2):174–188
10. Billi F, Campbell P (2010) Nanotoxicology of metal wear particles in total joint arthroplasty: a review of current concepts. *J Appl Biomater Biomech* 8(1):1–6
11. Gallo J et al (2013) Osteolysis around total knee arthroplasty: A review of pathogenetic mechanisms. *Acta Biomater* 9(9):8046–8058
12. Rituerto J, Hu X, Emami N (2013) Tribology, corrosion and tribocorrosion of metal on metal implants. *Tribology - Materials Surfaces & Interfaces* 7:1–12
13. Eltit F, Wang Q, Wang R (2019) Mechanisms of adverse local tissue reactions to hip implants. *Fronti Bioeng Biotechnol* 7:176
14. Hesketh J et al (2012) Tribocorrosion reactions between metal-on-metal and metal-on-polymer surfaces for total hip replacement. *Proceedings of the Institution of Mechanical Engineers, Part J: Journal of Engineering Tribology* 226(6):564–574
15. National Joint Registry 17th Annual Report 2020. 2020, National Joint Registry.
16. Hedberg YS (2018) Role of proteins in the degradation of relatively inert alloys in the human body. *Mater Degradat* 2(1):26
17. Espallargas N et al (2017) In-situ generated tribomaterial in metal/metal contacts: Current understanding and future implications for implants. *Biotribology* 10:42–50
18. Jacobs JJ, Gilbert JL, Urban RM (1998) Corrosion of metal orthopaedic implants. *J Bone Joint Surg Am* 80(2):268–282

19. Wimmer MA et al (2010) Wear mechanisms in metal-on-metal bearings: The importance of tribochemical reaction layers. *J Orthop Res* 28(4):436–443
20. Wimmer MA et al (2003) Tribochemical reaction on metal-on-metal hip joint bearings - A comparison between in-vitro and in-vivo results. *Wear* 255(2):1007–1014
21. Wimmer MA et al (2001) The acting wear mechanisms on metal-on-metal hip joint bearings: in vitro results. *Wear* 250(1):129–139
22. Wimmer, M. and A. Fischer, *Tribology. The adult hip*. 2007, Philadelphia: Lippincot Williams & Wilkins.
23. Pourzal R et al (2009) Micro-structural alterations within different areas of articulating surfaces of a metal-on-metal hip resurfacing system. *Wear* 267(5):689–694
24. Vinothkumar KR, Henderson R (2010) Structures of membrane proteins. *Q Rev Biophys* 43(1):65–158
25. Bradfield, P., J. Dodds, and N. Taylor (2001) *AS Level Biology*. Longman
26. Protein-surface interactions, in an introduction to tissue-biomaterial interactions. 2002. 37–52.
27. Malvern analytical. using raman spectroscopy to understand the conformational stability of protein therapeutics. AZoM, viewed 15 January 2020. viewed 15 January 2020; Available from: <https://www.azom.com/article.aspx?ArticleID=11142>.
28. Foley, S., et al. (2011) Photolysis of Bovine Serum Albumin by near UV irradiation
29. Maskiewicz VK et al (2010) Characterization of protein degradation in serum-based lubricants during simulation wear testing of metal-on-metal hip prostheses. *J Biomed Mater Res B Appl Biomater* 94(2):429–440
30. Lewis EN et al (2014) Combined dynamic light scattering and Raman spectroscopy approach for characterizing the aggregation of therapeutic proteins. *Molecules (Basel, Switzerland)* 19(12):20888–20905
31. Thawornchinsombut S et al (2006) Raman spectroscopy determines structural changes associated with gelation properties of fish proteins recovered at alkaline pH. *J Agric Food Chem* 54(6):2178–2187
32. Zhang S et al (2012) Raman spectroscopic characterization of structural changes in heated whey protein isolate upon soluble complex formation with pectin at near neutral pH. *J Agric Food Chem* 60(48):12029–12035
33. Wang C-H et al (2016) The effect of disulfide bonds on protein folding, unfolding, and misfolding investigated by FT-Raman spectroscopy. *J Raman Spectrosc* 47(8):940–947
34. Chen MC, Lord RC (1976) Laser-excited raman spectroscopy of biomolecules VIII Conformational study of bovine serum albumin. *J Am Chem Soc* 98(4):990–992
35. Weselucha-Birczyńska A et al (2013) Raman micro-spectroscopy tracing human lymphocyte activation. *Analyst* 138:7157
36. Esmonde-White KA et al (2009) Raman spectroscopy of synovial fluid as a tool for diagnosing osteoarthritis. *J Biomed Opt* 14(3):034013
37. Lin VJC, Koenig JL (1976) Raman studies of bovine serum albumin. *Biopolymers* 15(1):203–218
38. Muñoz AI, Mischler S (2015) Electrochemical Quartz Crystal Microbalance and X-Ray Photoelectron Spectroscopy study of cathodic reactions in Bovine Serum Albumin containing solutions on a Physical Vapour Deposition-CoCrMo biomedical alloy. *Electrochim Acta* 180:96–103
39. Muñoz AI, Mischler S (2007) Interactive effects of albumin and phosphate ions on the corrosion of CoCrMo implant alloy. *J Electrochem Soc* 154(10):C562–C570
40. Munoz AI, Mischler S (2011) Effect of the environment on wear ranking and corrosion of biomedical CoCrMo alloys. *J Mater Sci Mater Med* 22(3):437–450
41. Hesketh J et al (2014) The composition of tribofilms produced on metal-on-metal hip bearings. *Biomaterials* 35(7):2113–2119
42. Bergmann G et al (2012) High-tech hip implant for wireless temperature measurements In Vivo. *PLoS ONE* 7(8):43489
43. Liang M et al (2006) A simple and direct isolation of whey components from raw milk by gel filtration chromatography and structural characterization by Fourier transform Raman spectroscopy. *Talanta* 69(5):1269–1277
44. Namus R et al (2020) The influence of protein concentration, temperature and cathodic polarization on the surface status of CoCrMo biomedical grade alloys. *Appl Surf Sci* 499:143908
45. Valero Vidal C, Olmo Juan A, Igual Muñoz A (2020) Adsorption of bovine serum albumin on CoCrMo surface Effect of temperature and protein concentration. *Colloids and Surfaces Biointerfaces* 80(1):1–11
46. ASTM International, ASTM F75 - 12, in Standard Specification for Cobalt-28 Chromium-6 Molybdenum Alloy Castings and Casting Alloy for Surgical Implants (UNS R30075). 2012: West Conshohocken, PA
47. Swaminathan V, Gilbert JL (2012) Fretting corrosion of CoCrMo and Ti6Al4V interfaces. *Biomaterials* 33(22):5487–5503
48. Yoneyama C et al (2020) Influence of bovine serum albumin (BSA) on the Tribocorrosion behaviour of a low carbon CoCrMo Alloy in simulated body fluids. *Lubricants* 8(5):61
49. Namus R, Rainforth WM (2020) Influence of protein adsorption on tribocorrosion behaviour of CoCrMo biomedical-grade alloys. *Tribol Int* 150:106364
50. Sadiq K, Stack MM, Black RA (2015) Wear mapping of CoCrMo alloy in simulated bio-tribocorrosion conditions of a hip prosthesis bearing in calf serum solution. *Mater Sci Eng, C* 49:452–462
51. International, A. (2014) *ASTM G5*, in Standard Reference Test Method for Making Potentiodynamic Anodic Polarization Measurements West Conshohocken PA
52. International, A., *ASTM G59–97*, in Standard Test Method for Conducting Potentiodynamic Polarization Resistance Measurements. 2020: West Conshohocken, PA
53. Anissian HL et al (2001) The wear pattern in metal-on-metal hip prostheses. *J Biomed Mater Res* 58(6):673–678
54. Smith SL, Dowson D, Goldsmith AAJ (2001) The lubrication of metal-on-metal total hip joints: A slide down the Stribeck curve. *Proceedings of the Institution of Mechanical Engineers* 215(5):483–493
55. Beadling AR et al (2016) Tribocorrosion of hard-on-hard total hip replacements with metal and ceramic counterfaces under standard and adverse loading conditions. *Tribol Int* 103:359–367
56. Myant C et al (2012) Lubrication of metal-on-metal hip joints: The effect of protein content and load on film formation and wear. *J Mech Behav Biomed Mater* 6:30–40
57. International Organization for Standardization, ISO 14243–3:2004, in Implants for surgery - Wear of total knee-joint prostheses - Part 3: Loading and displacement parameters for wear-testing machines with displacement control and corresponding environmental conditions for test 2004. 2004
58. Hesketh J et al (2013) Biotribocorrosion: Some electrochemical observations from an instrumented hip joint simulator. *Tribol Int* 59:332–338
59. Hesketh, J.E.T. (2012) *Tribocorrosion of total hip replacements*. University of Leeds.
60. International, A. (2021) *ASTM G119–09*, in standard guide for determining synergism between wear and corrosion. West Conshohocken PA
61. Beadling, A.R. (2016) *Biotribocorrosion of hard-on-hard bearing surfaces in orthopaedic Hip replacements*. University of Leeds
62. Oladokun, A. (2017) *Mechanism of fretting corrosion at the modular taper interface of hip prosthesis*. University of Leeds

63. Bryant, M. (2013) Fretting-crevice corrosion of cemented metal on metal total hip replacements. University of Leeds
64. Pocock G., CD Richards (2009) The human body: an introduction for the biomedical and health sciences. Oxford University Press
65. Sinnett-Jones PE, Wharton JA, Wood RJK (2005) Micro-abrasion–corrosion of a CoCrMo alloy in simulated artificial hip joint environments. *Wear* 259(7):898–909
66. Hutchings, I, P Shipway (2017) Tribology Friction and wear of engineering materials Second Edition Elsevier pp 1–388.
67. Archard JF (1953) Contact and rubbing of flat surfaces. *J Appl Phys* 24(8):981–988
68. Mischler S (2008) Triboelectrochemical techniques and interpretation methods in tribocorrosion: A comparative evaluation. *Tribol Int* 41(7):573–583
69. Stack MM, Mathew MT, Hodge C (2011) Micro-abrasion–corrosion interactions of Ni–Cr/WC based coatings: Approaches to construction of tribo-corrosion maps for the abrasion–corrosion synergism. *Electrochim Acta* 56(24):8249–8259
70. Stack MM et al (2011) Some views on the construction of biotribo-corrosion maps for Titanium alloys in Hank’s solution: Particle concentration and applied loads effects. *Tribol Int* 44(12):1827–1837
71. Yan Y et al (2010) Tribofilm formation in biotribo-corrosion – does it regulate ion release in metal-on-metal artificial hip joints? Proceedings of the Institution of Mechanical Engineers, Part J: Journal of Engineering Tribology 224(9):997–1006
72. Bryant M, Neville A (2017) Fretting corrosion of CoCr alloy: Effect of load and displacement on the degradation mechanisms. *Proc Inst Mech Eng [H]* 231(2):114–126
73. Mischler S, Muñoz AI (2013) Wear of CoCrMo alloys used in metal-on-metal hip joints: A tribocorrosion appraisal. *Wear* 297(1):1081–1094
74. Mishina H, Kojima M (2008) Changes in human serum albumin on arthroplasty frictional surfaces. *Wear* 265(5):655–663
75. Williams DF, Askill IN, Smith R (1985) Protein absorption and desorption phenomena on clean metal surfaces. *J Biomed Mater Res* 19(3):313–320
76. Contu F, Elsener B, Böhni H (2003) Characterization of implant materials in fetal bovine serum and sodium sulfate by electrochemical impedance spectroscopy II Coarsely sandblasted samples. *J Biomed Mater Res A* 67(1):246–254
77. Wimmer M et al (2006) Investigation on stick phenomena in metal-on-metal hip joints after resting periods. *Proc Inst Mech Eng [H]* 220(2):219–227
78. Donnet C et al (1996) Super-low friction of MoS₂ coatings in various environments. *Tribol Int* 29(2):123–128
79. Farr JPG (1975) Molybdenum disulphide in lubrication. A Review *Wear* 35(1):1–22
80. Qian W, Krimm S (1992) Vibrational studies of the disulfide group in proteins VII Normal mode analysis of the Raman spectra of erabutoxin, γ -II crystallin and immunoglobulin. *J Raman Spectro* 23(10):517–521
81. Thornley B et al (2020) Investigation into the repassivation process of CoCrMo in a simulated biological environment. *Corrosion* 76:539–552
82. Sun D, Wharton JA, Wood RJK (2009) Micro-abrasion mechanisms of cast CoCrMo in simulated body fluids. *Wear* 267(11):1845–1855
83. Sun D, Wharton J, Wood R (2010) The effects of protein and pH on the tribo-corrosion performance of cast CoCrMo — a combined electrochemical and tribological study. *Advanced Tribology*. https://doi.org/10.1007/978-3-642-03653-8_272
84. Valero Vidal C, Igual Muñoz A (2008) Electrochemical characterisation of biomedical alloys for surgical implants in simulated body fluids. *Corrosion Sci* 50(7):1954–1961
85. Rodríguez GR, Aperador WJN-DT (2016) Remote monitoring technique for evaluation of corrosion on reinforced concrete structures. *Non-Destruct Test*. <https://doi.org/10.5772/62314>
86. Romano P et al (2013) Monitoring of the degradation of concrete structures in environments containing. *Chloride Ions* 47:827–832
87. Vidal CV et al (2012) Passivation of a CoCrMo PVD alloy with biomedical composition under simulated physiological conditions studied by EQCM and XPS. *J Electrochem Soc* 159(5):C233–C243
88. Kerwell S et al (2017) Electrochemically induced film formation on CoCrMo alloy for hip implant application. *J Bio Tribo Corros*. <https://doi.org/10.1007/s40735-016-0063-y>
89. Wang Z et al (2017) Effect of electrochemical corrosion on the subsurface microstructure evolution of a CoCrMo alloy in albumin containing environment. *Appl Surf Sci* 406:319–329
90. Mathew MT, Jacobs JJ, Wimmer MA (2012) Wear-corrosion synergism in a CoCrMo hip bearing alloy is influenced by proteins. *Clin Orthop Relat Res* 470(11):3109–3117
91. Bryant M et al (2014) Galvanically enhanced fretting-crevice corrosion of cemented femoral stems. *J Mech Behav Biomed Mater* 40:275–286
92. López-Ortega A, Arana JL, Bayón R (2018) Tribocorrosion of passive materials: a review on test procedures and standards. *Int J Corrosion* 2018:7345346
93. Jellesen MS et al (2009) Erosion–corrosion and corrosion properties of DLC coated low temperature gas-nitrided austenitic stainless steel. *Wear* 267(9):1709–1714
94. Callow LM, Richardson JA, Dawson JL (1976) Corrosion monitoring using polarisation resistance measurements: I techniques and correlations. *Br Corros J* 11(3):123–131
95. Callow LM, Richardson JA, Dawson JL (1976) Corrosion monitoring using polarisation resistance measurements: II Sources of error. *Br Corros J* 11(3):132–139
96. Contu F, Elsener B, Böhni H (2003) Electrochemical behavior of CoCrMo alloy in the active state in acidic and alkaline buffered solutions. *J Electrochem Soc* 150(9):B419
97. International, A., ASTM F746–04, in Standard Test Method for Pitting or Crevice Corrosion of Metallic Surgical Implant Materials. 2009: West Conshohocken, PA.
98. Zhang XL et al (2009) Effects of scan rate on the potentiodynamic polarization curve obtained to determine the Tafel slopes and corrosion current density. *Corros Sci* 51(3):581–587
99. Silverman DC (1998) Tutorial on cyclic potentiodynamic polarization technique. *Corrosion* 98:1998

Publisher's Note Springer Nature remains neutral with regard to jurisdictional claims in published maps and institutional affiliations.